Selective, High-Temperature O_2 Adsorption in Chemically Reduced, Redox-Active Iron-Pyrazolate Metal–Organic Frameworks

Adam Jaffe,[†] Michael E. Ziebel,[†,§] David M. Halat,[‡,§] Naomi Biggins,[†,§] Ryan A. Murphy,[†] Khetpakorn Chakarawet,[†] Jeffrey A. Reimer,[‡,§] and Jeffrey R. Long*[,†,‡,§]

[†]Department of Chemistry and [‡]Department of Chemical and Biomolecular Engineering, University of California, Berkeley, California 94720, United States

[§]Materials Sciences Division, Lawrence Berkeley National Laboratory, Berkeley, California 94720, United States

ABSTRACT: Developing O_2-selective adsorbents that can produce high-purity oxygen from air remains a significant challenge. Here, we show that chemically reduced metal–organic framework materials of the type $A_xFe_2(bdp)_3$ ($A = Na^+$, K^+; bdp^{2-} = 1,4-benzenedipyrazolate; $0 < x \leq 2$), which feature coordinatively saturated iron centers, are capable of strong and selective adsorption of O_2 over N_2 at ambient (25 °C) or even elevated (200 °C) temperature. A combination of gas adsorption analysis, single-crystal X-ray diffraction, magnetic susceptibility measurements, and a range of spectroscopic methods, including ^{23}Na solid-state NMR, Mössbauer, and X-ray photoelectron spectroscopies, are employed as probes of O_2 uptake. Significantly, the results support a selective adsorption mechanism involving outer-sphere electron transfer from the framework to form superoxide species, which are subsequently stabilized by intercalated alkali metal cations that reside in the one-dimensional triangular pores of the structure. We further demonstrate similar O_2 uptake behavior to that of $A_xFe_2(bdp)_3$ in an expanded-pore framework analogue and thereby gain additional insight into the O_2 adsorption mechanism. The chemical reduction of a robust metal–organic framework to render it capable of binding O_2 through such an outer-sphere electron transfer mechanism represents a promising and underexplored strategy for the design of next-generation O_2 adsorbents.

Introduction

The isolation of high-purity oxygen from air is vital for pre-combustion (i.e., carbonaceous fuel gasification) and post-combustion (i.e., oxy-fuel combustion) carbon capture technologies,[1] as well as for the steel, medical, chemical, food, glass, and waste-treatment industries.[2] Currently, purification methods such as cryogenic distillation are carried out on a large scale in industry, although these separations require enormous energy inputs.[2,3] On smaller scales, membranes can increase O_2 concentrations relative to air, but they are typically capable of only ~50% enrichment.[3] Porous adsorbents stand as attractive alternatives for O_2 purification, given that they can operate with high energy efficiencies and therefore at lower cost than low-temperature methods. However, the cation-exchanged zeolites currently employed in adsorbent-based air separation are generally N_2-selective[4,5] and must be regenerated frequently, owing to the larger nitrogen fraction in air (78%) compared with oxygen (21%). Furthermore, the purity of oxygen derived from these zeolite adsorbents is also typically limited to ≤95%.[3,5]

The development of an O_2-selective adsorbent, especially one capable of separating oxygen at ambient or elevated temperature, could both enhance efficiency for this important industrial separation and facilitate technologies that mediate CO_2 release into the atmosphere. Indeed, in pre-combustion carbon capture—where carbonaceous fuel is gasified using high-purity O_2, converted to syngas, and combusted to power a turbine—significant efficiency gains are achieved by feeding air to the separation unit directly from the turbine compressor.[3,6,7] In this integrated gasification combined cycle, air from the turbine compressor can exceed 300 °C due to compressive heating, and this heat must be rejected before entering the separation unit.[3] Consequently, substantial energy savings could be achieved using an air separation unit capable of operating well above ambient temperature.

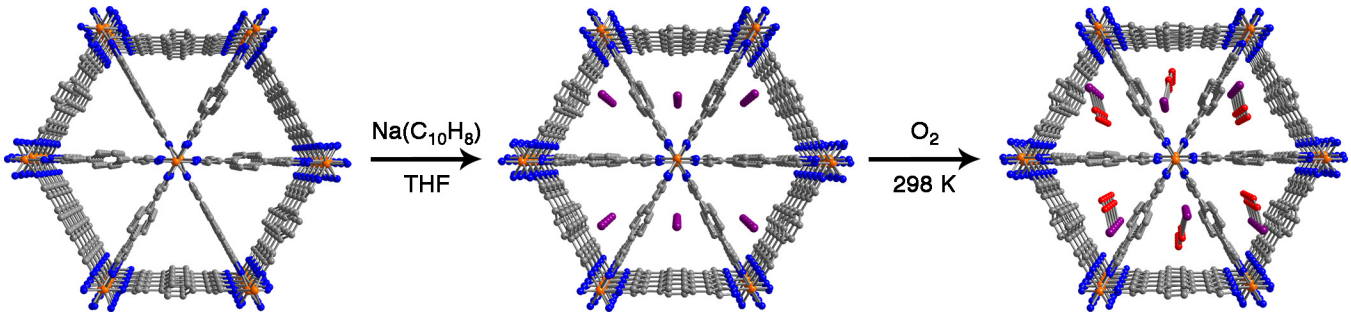

Figure 1. X-ray crystal structures of $Fe_2(bdp)_3$ (left), $Na_{0.5}Fe_2(bdp)_3$ (middle), and room-temperature O_2-dosed $Na_{1.2}Fe_2(bdp)_3$ (right). Orange, blue, gray, red, and purple spheres represent Fe, N, C, O, and Na atoms, respectively. Disordered atoms and H atoms are omitted for clarity.

The design of O_2-selective adsorbents is particularly challenging given the similar physical properties of O_2 and N_2, such as kinetic diameter, polarizability, and quadrupole moment.[8] Nitrogen is slightly greater in both polarizability and quadrupole moment—factors that are exploited by N_2-selective zeolites. Redox activity, however, is perhaps the most powerful characteristic of O_2 that distinguishes it from N_2. Indeed, biological systems leverage strategies based on redox-activity to reversibly bind dioxygen,[9] and similar behavior has been engineered in synthetic complexes[10-12] and porous metal–organic frameworks through the use of coordinatively unsaturated, redox-active metal centers that provide open binding sites for O_2. Depending on the electronic properties of the metal centers and the coordination environments in these systems, O_2 can be reduced to either a superoxo (O_2^-) or peroxo (O_2^{2-}) species and can exhibit a variety of binding modes.

Given their high tunability, crystallinity, and chemical versatility,[8,13-22] metal–organic frameworks can provide appealing platforms for the design of O_2-selective adsorbents. Indeed, frameworks such as $Cr_3(btc)_2$ (btc^{3-} = 1,3,5-benzenetricarboxylate),[23] Cr-BTT (BTT^{3-} = 1,3,5-benzenetristetrazolate),[24] $Fe_2(dobdc)$ ($dobdc^{4-}$ = 2,5-dioxido-1,4-benzenedicarboxylate),[25] Co-BTTri (H_3BTTri = 1,3,5-tri(1*H*-1,2,3-triazol-5-yl)benzene),[26] and PCN-224Mn^{II} [27] have shown high selectivities and capacities for O_2. However, oxygen binding in many of these materials is either irreversible or very weak at ambient temperature, and the frameworks tend to suffer from poor thermal stability, capacity loss during cycling, or framework degradation under humid conditions. Given that only a small fraction of all reported metal–organic frameworks feature open metal sites and the tunable design of such frameworks remains a considerable challenge, it is crucial to explore alternate design strategies.

To improve the energy efficiency of air separation processes, an ideal adsorbent would be highly selective for O_2 and stable at ambient and even elevated temperature. In seeking underexplored O_2 adsorption routes, we considered the possibility of *outer-sphere* electron transfer from coordinatively *saturated*, redox-active metal centers (Figure 1). Here, post-synthetic chemical reduction of a stable framework is expected to generate a material capable of reducing O_2 that would also feature charge-balancing cations for stabilizing the reduced O_2 species. Beyond the choice of metal and ligand, these cations could also offer an additional functional handle for tuning adsorption properties. Such a strategy requires a material with redox-active centers, the potential for topotactic insertion of charge-balancing cations, chemical resistance to reactive O_2^{n-} species, and high thermal stability. We therefore turned to the framework $Fe_2(bdp)_3$ (bdp^{2-} = 1,4-benzenedipyrazolate),[28] which is known to undergo chemical reduction with potassium naphthalenide to yield $K_xFe_2(bdp)_3$ ($0 < x \leq 2$).[29] This material and a related Fe^{II}-tetrazolate framework have been described as exhibiting reactivity in air,[29,30] but their O_2 adsorption properties were not investigated further. Herein, we show that the materials $A_xFe_2(bdp)_3$ (A = Na^+, K^+; $0 < x \leq 2$, Figure 1) are capable of selectively adsorbing O_2 over N_2 with high capacities at room temperature and as high as 200 °C and that they can be partially regenerated using heat and vacuum. Comprehensive characterization methods, including gas adsorption measurements, single-crystal X-ray diffraction, and numerous solid-state spectroscopies, provide evidence that O_2 is reduced to a superoxo species upon adsorption, ostensibly via an outer-sphere electron transfer mechanism. These results are the first illustration of the use of chemical reduction of a stable framework to generate new high-performance adsorbents capable of exceptionally selective O_2 capture.

Results and Discussion

Synthesis and Characterization.

The synthesis of $Fe_2(bdp)_3$ was performed following the previously reported procedure[28] to afford a black microcrystalline solid. The structure of this material consists of one-dimensional μ^2-pyrazolate-bridged chains of octahedrally coordinated iron(III) nodes, connected in three dimensions by bdp^{2-} linkers to yield a rigid framework with triangular channels (Figure 1). Importantly, the strong metal–pyrazolate bonds and structural rigidity of the framework should serve to prevent coordinative reorganization or material degradation upon O_2 adsorption.

Subsequent reduction of $Fe_2(bdp)_3$ with sodium or potassium naphthalenide in tetrahydrofuran yielded $A_xFe_2(bdp)_3$ (A = Na^+, K^+; $0 < x \leq 2$) in a topotactic manner, as previously described.[29] Langmuir surface areas of 750–790 m^2/g were reliably obtained for the half-reduced framework materials $AFe_2(bdp)_3$ following activation at 180 °C, whereas the fully reduced compound $A_2Fe_2(bdp)_3$ was found to be essentially non-porous to N_2. We therefore narrowed our initial focus to the half-reduced form of this framework due to its greater accessible porosity.[29] Additionally, on the basis of its electrochemical behavior, $AFe_2(bdp)_3$ is less reducing than $A_2Fe_2(bdp)_3$,[29] which should favor the formation of superoxo rather than peroxo species. We note that, because superoxide is a one-electron reduction product of O_2, a material that favors an alkali-stabilized superoxo species in its pores has twice the theoretical capacity of one that generates a peroxo species. Superoxo binding is also more likely to be reversible than peroxo binding, and indeed peroxo binding is often irreversible—as has been observed at elevated temperature for $Fe_2(dobdc)$.[25] We further focused our initial studies on the potassiated congener, due to the relative stability of potassium superoxide compared to sodium superoxide.[31-33]

O_2 Adsorption in Reduced $Fe_2(bdp)_3$.

We initially probed the interaction of reduced $Fe_2(bdp)_3$ with dioxygen by measuring the O_2 adsorption isotherm of $K_{1.09}Fe_2(bdp)_3$ at 298 K (Figure 2). Powder X-ray diffraction data collected at this temperature confirmed no loss of crystallinity or change in symmetry upon O_2 dosing (Figure S1). At low pressures, the material exhibits extraordinarily steep uptake

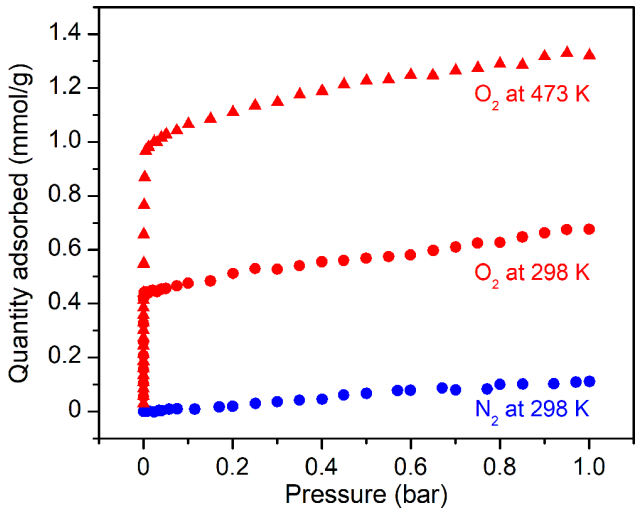

Figure 2. Adsorption isotherms for the uptake of O_2 and N_2 at 298 K (red and blue circles, respectively) and O_2 at 473 K (triangles) in $K_{1.09}Fe_2(bdp)_3$.

of O_2 (Figure 2), achieving a loading of 0.44 mmol/g at just 1 mbar O_2. The O_2 uptake thereafter rises only gradually with increasing pressure, resulting in a loading of 0.51 mmol/g at 0.21 bar—close to the partial pressure of O_2 in air—and a maximum loading of 0.68 mmol/g at 1 bar. The steep O_2 uptake is suggestive of strong initial adsorption, whereas in contrast, $K_{1.09}Fe_2(bdp)_3$ exhibits little N_2 adsorption under these conditions, consistent with only weak physisorptive guest–framework interactions. The O_2 and N_2 adsorption isotherms were modeled using multi-site and single-site Langmuir-Freundlich equations, respectively (Figure S2; see details in Supporting Information), and the strong interaction of the framework with O_2 is exemplified by far higher Langmuir parameter values (Table S1). Given the stark differences in the O_2 and N_2 adsorption profiles, we would further expect substantial selectivity for O_2 over N_2 under the measured conditions. The direct calculation of selectivities using Ideal Adsorbed Solution Theory is not applicable here, however, as this theory poorly predicts adsorption equilibria for mixtures containing adsorbates with substantially differing adsorption interactions and for adsorbents with heterogenous surfaces, such as cation-exchanged zeolites.[34,35]

The framework capacity at 0.21 bar of O_2 corresponds to approximately 40% of the theoretical capacity (1.40 mmol/g) given a stoichiometry of $K_{1.09}Fe_2(bdp)_3$ and assuming one-electron reduction of O_2 to form superoxo species. This result implies that either a more reduced dioxygen species is being formed or there is a kinetic barrier to complete O_2 loading. Indeed, if the O_2 uptake at ambient temperature is kinetically limited, a substantial increase in available thermal energy could surmount the activation barrier and enable access to the full capacity of the material, assuming no change in the mechanism of adsorption. Examples of kinetic limitations could include hindered diffusion through the narrow triangular framework channels due to occlusion by reduced O_2 species, an activation barrier toward rearrangement of alkali cations upon introduction of O_2, sluggish movement of reduced O_2 species to preferred binding sites, or even a barrier to electron transfer.

Seeking to explain this partial loading, as well as to test the chemical stability of the material, we further measured O_2 adsorption at 473 K (200 °C). Significantly, $K_{1.09}Fe_2(bdp)_3$ retains its strong affinity for O_2 at this temperature and displays an enhanced adsorption capacity (Figure 2), achieving a loading of 0.98 mmol/g at 10 mbar. Subsequent dosing yielded loadings of 1.11 and 1.32 mmol/g at close to 0.21 and 1.0 bar, respectively. The uptake at 0.21 bar of O_2 corresponds to ~80% of the theoretical capacity, which critically rules out the formation of a peroxo species, at least at 473 K. Based on these data, we again expect the O_2/N_2 selectivity of $K_{1.09}Fe_2(bdp)_3$ at 473 K to be extraordinarily high. The apparent selectivity of this material for O_2 at ambient temperature and the substantial increase in capacity at such a high temperature ultimately indicate its great promise for O_2 separations.

Desorption isotherms collected for $K_{1.09}Fe_2(bdp)_3$ at 298 K show only the release of weakly bound O_2 (Figure S3), while the majority remains strongly adsorbed. A small amount of hysteresis is observed, likely due to strong but highly kinetically limited binding of O_2 during the shallow uptake region of the adsorption isotherm that is not removed upon desorption. However, upon heating to 453 K (180 °C) under vacuum after an adsorption and desorption isotherm cycle, the material can be partially regenerated. Over at least five adsorption/desorption cycles between 0 and 0.21 bar at 298 K followed by activation, the quantity of O_2 adsorbed during each adsorption isotherm appears to reach an asymptotic value of ~0.2 mmol/g (Figure S4). We note that the regeneration conditions were not optimized, and indeed we found that heating to 478 K (205 °C) under vacuum resulted in greater capacity recovery. Thus, higher regeneration temperatures and longer regeneration times may allow for more of the capacity of the material to be recovered. In fact, desorption at 473 K appears to be more reversible in the low-pressure region than at 298 K (Figure S5), and impressively the material can be cycled at least 10 times at these elevated temperatures, albeit with diminished capacities (Figure S6).

We also measured 298 and 473 K O_2 adsorption isotherms for $Na_{1.04}Fe_2(bdp)_3$ (Figure S7), which displayed almost identical behavior to the potassiated version. Thus, the stability of the reduced O_2 species within the framework pores appears not to be strongly dependent on the alkali metal cation, although complex cations could show different behavior.

The foregoing results imply that the adsorption of O_2 in $A_xFe_2(bdp)_3$ is either under kinetic control to some degree or that the mechanism of O_2 adsorption is altered at elevated temperature. We therefore sought a deeper understanding of (i) the lower O_2 uptake at ambient temperature—for example, whether O_2 diffusion is limited as described above and (ii) the nature of the adsorbed O_2 species.

Single-Crystal X-ray Structure Determinations.

Single-crystal X-ray diffraction was employed to determine the nature of the adsorbed O_2 species in $A_xFe_2(bdp)_3$ and the adsorption mechanism. Dark, acicular, X-ray quality single crystals of $Fe_2(bdp)_3$ were synthesized using a modification[36] of the original synthetic procedure (see Supporting Information).[29] Following chemical reduction, activation, and room temperature O_2 dosing of the crystals (details available in the Supporting Information), we obtained structures of both Na- and K-reduced $Fe_2(bdp)_3$ (Figures 1 and 3). Virtually the same Fe–N bond lengths and ligand metrical parameters were found for reduced $Fe_2(bdp)_3$ and its O_2-dosed form; however, the pores of the latter structure are clearly occupied by O_2 species stabilized by intercalated cations. We note that the absence of observable O_2 species near the iron centers also helps refute the possibility that O_2 binding is simply occurring at defect sites. Attempts to collect structural data following O_2 dosing at 473 K revealed that the material was not sufficiently crystalline for a structure determination.

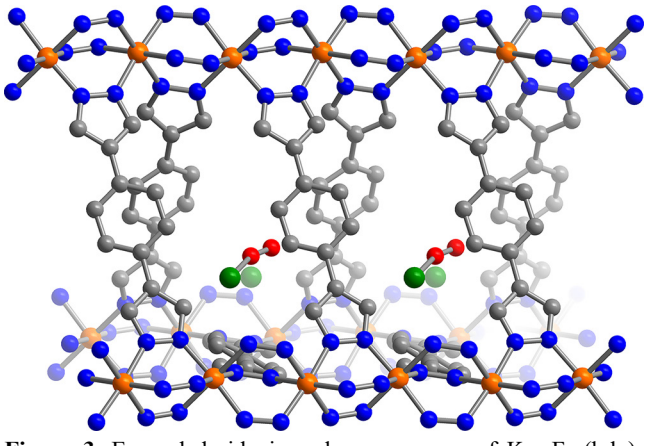

Figure 3. Expanded sideview along one pore of $K_{0.74}Fe_2(bdp)_3$ dosed with 1 bar O_2 at 298 K. Orange, gray, blue, red, and green spheres represent Fe, C, N, O, and K atoms, respectively. Both crystallographically distinct K sites are shown. Disordered atoms created by symmetry and hydrogen atoms are omitted for clarity.

The diffraction data collected for crystals dosed with O_2 at 298 K were best modeled assuming two crystallographically unique Na^+ or K^+ ion sites. One position is very similar to the cation site near the phenyl groups of the ligand in the reduced, activated structures.[36] Indeed, for both O_2-dosed structures, the alkali metal ion···phenyl-centroid distances are 3.44(2) Å, compared with 3.429(4) Å in activated $Na_{0.5}Fe_2(bdp)_3$. The second alkali metal position—with longer alkali metal ion···phenyl-centroid distances of 3.87(2) and 3.88(2) Å for sodium and potassium, respectively—appears to stabilize the O_2 species, with a Na–O distance of 2.30(3) Å and a K–O distance of 2.31(3) Å. The distances between the two crystallographically distinct alkali sites are 1.21(3) Å (sodiated structure) and 1.24(3) Å (potassiated structure). The O_2 species and alkali metal ion sites reside near an inversion center at the middle of the triangular pore and are thus duplicated by symmetry. Importantly, the O–O distances of 1.29(6) and 1.34(6) Å in the sodiated and potassiated structures, respectively, are consistent with reported bond lengths for superoxo species.[33] The closest pyrazolate N···O distances are 5.81(2) and 5.79(2) Å for A = Na^+ and K^+, respectively, whereas the corresponding Fe···O distances are 7.16(2) and 7.14(2) Å. Assuming that outer-sphere electron transfer occurs at a point of closer contact, these relatively large distances between the iron–nitrogen coordination sphere and oxygen atoms imply that substantial rearrangement and movement of the reduced O_2 species must occur following electron transfer.

We note that both the crystal symmetry and stoichiometry necessitate partial occupancy of the alkali metal and O atom crystallographic sites. Additional factors, such as structural disorder, the proximity of adsorbed O_2 to a point of high symmetry in the center of the pore, large thermal motion, and the relatively low electron density of these species, make a precise determination of the O–O bond length and other distances difficult. However, these structures conclusively show the presence of adsorbed O_2 species and are consistent with an adsorption mechanism involving one-electron reduction of O_2.

Analysis of Extra-Framework Species.

Vibrational spectroscopy is often used to probe the nature of reduced O_2 species given that the bond order and therefore the vibrational frequency of the O–O bond are distinct for O_2^- and O_2^{2-}. However, despite numerous attempts, we were unable to assign any O–O signatures using Raman or *in situ* diffuse reflectance infrared spectroscopy (see the Supporting Information for details). We therefore utilized X-ray photoelectron spectroscopy (XPS) and solid-state NMR spectroscopy coupled with density functional theory (DFT) calculations to further elucidate the nature of the O_2 species adsorbed in $AFe_2(bdp)_3$ and the associated chemical environment of the alkali metal cations.

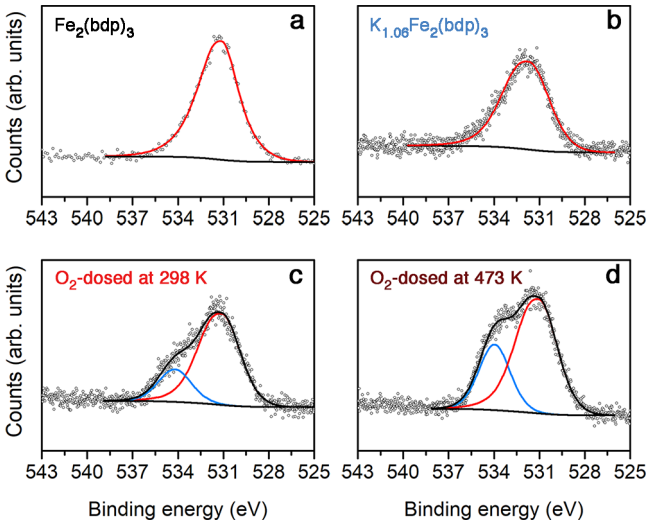

Figure 4. Oxygen 1s XPS spectra for (a) $Fe_2(bdp)_3$, (b) $K_{1.06}Fe_2(bdp)_3$, and $K_{1.06}Fe_2(bdp)_3$ dosed with 1 bar O_2 at (c) 298 and (d) 473 K. Individual peak fits are shown in red and blue. Peak fit backgrounds and envelopes are shown with black lines.

Owing to the strongly bound nature of the O_2 species in these materials, we were able to directly compare the O 1s signals in $Fe_2(bdp)_3$, $K_{1.06}Fe_2(bdp)_3$, and $K_{1.06}Fe_2(bdp)_3$ dosed with 1 bar O_2 at either 298 or 473 K, under the high vacuum of the XPS measurement chamber. As previously reported,[29] $Fe_2(bdp)_3$ contains defects likely associated with ligand vacancies. For this material, we observe an O 1s signal that we accordingly assign to oxygen-containing defect species at a binding energy of 531.1 eV (Figure 4), consistent with hydroxides or oxygen-containing organics such as formate.[37-42] This peak is also observed at a similar binding energy in $K_{1.06}Fe_2(bdp)_3$, as well as in both O_2-dosed $K_{1.06}Fe_2(bdp)_3$ samples. Critically, for both of these O_2-dosed samples, a new O 1s peak is also present at a higher binding energy of ~534.1 eV, consistent with a superoxo, rather than more reduced peroxo or oxo species.[37,40,42-45] The observation of this new peak for both samples suggests that (i) the nature of the reduced, adsorbed O_2 species is the same, regardless of dosing temperature, and (ii) the mechanism of O_2 adsorption is therefore likely also the same. As such, differences in O_2 adsorption capacity at 298 and 473 K most likely arise from kinetics effects. Furthermore, the relative area of this higher energy peak is greater for the sample dosed with O_2 at high temperature, as expected given the greater O_2 loading with increasing temperature. As further corroboration of this signal assignment, we measured the O 1s spectrum of potassium superoxide (KO_2) and observe a similar binding of energy of 533.8 eV (Figure S8).

We turned to solid-state magic-angle spinning (MAS) NMR spectroscopy as a more sensitive probe of local structural changes occurring upon O_2 dosing, and chose to study the Na analogue due to the greater ease of obtaining ^{23}Na data compared to ^{39}K NMR data. Typically, NMR spectroscopy of paramagnetic systems is challenging due to hyperfine interactions between unpaired electrons and the NMR-active nucleus. These interactions may be isotropic and through-bond (Fermi contact) and/or anisotropic and through-space (hyperfine dipolar coupling), often leading to large NMR shifts and highly broadened spectral features.[46] For example, the highest frequency ^{23}Na shift of Na_2FePO_4F is 450 ppm—well outside the typical diamagnetic range of −50 to 100 ppm. In this case, unpaired spin density is transferred along bond pathways from the Fe through O and onto Na.[47] On the other hand, in some paramagnetic systems, the Fermi contact shift may be unusually small due to competition between delocalization and polarization mechanisms. In NaO_2, where superoxide acts as the paramagnetic center, the room-temperature ^{23}Na shift is only –30 ppm.[48]

The ^{23}Na MAS NMR spectra for activated $Na_{1.04}Fe_2(bdp)_3$ and for aliquots of the same sample after dosing with O_2 at 298 K and at 473 K, are shown in Figure 5a. Given the large signal width resulting from paramagnetic broadening, data collection required the use of variable-offset cumulative spectroscopy (VOCS), wherein spin echo sub-spectra are acquired at spaced frequency offsets and summed together.[49] Two features are consistently observed in these spectra: a relatively sharp feature centered at −12 ppm with associated spinning sideband manifold and a very broad signal centered at ~50 ppm, which is somewhat obscured by the first signal. Baseline subtractions of

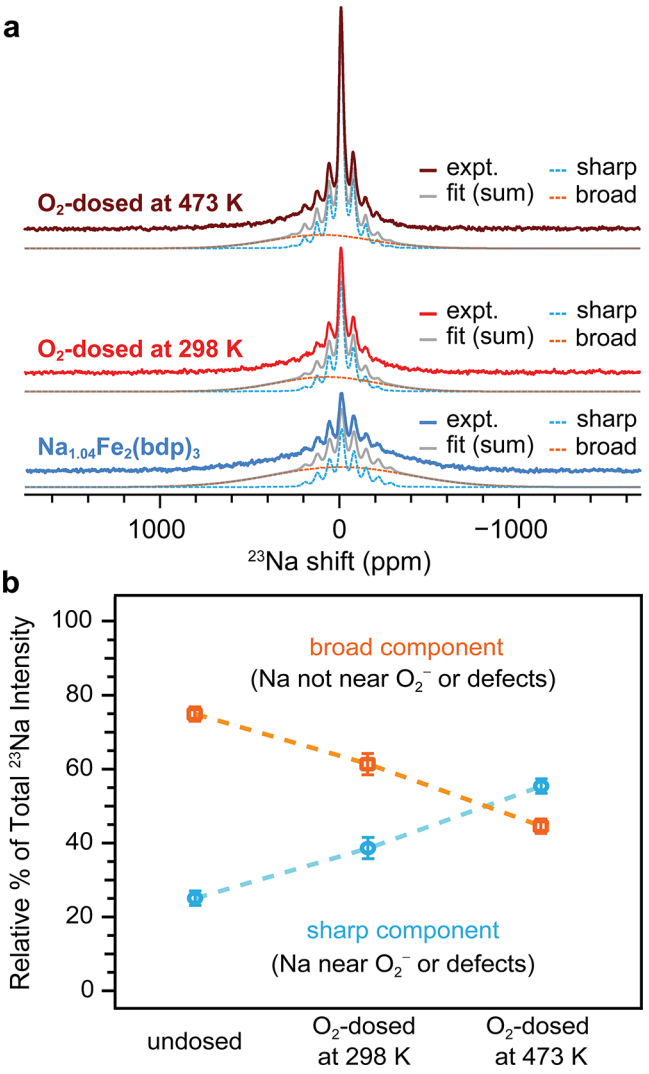

Figure 5. (a) ^{23}Na VOCS MAS NMR spectra of activated $Na_{1.04}Fe_2(bdp)_3$ (solid blue curve) and the same material dosed with 1 bar O_2 at 298 and at 473 K (red and dark red, respectively); spectra were acquired at 11.7 T at a MAS rate of 9 kHz. The ^{23}Na NMR spectra are deconvoluted (vertically offset for comparison) into broad and sharp components, the latter including a fitted spinning sideband manifold. Difference plots are shown in Figure S9. (b) Quantitative relative intensities of the deconvoluted spectral features as a function of dosing condition. Dashed lines are guides for the eye.

the sub-spectra were performed to ensure that the intensity of the broad feature was accurate. Moreover, neither signal was observed in control experiments with an empty probe, confirming they arose from Na within the sample.

Spectral deconvolutions shown in Figures 5a and S9 strongly suggest that the sharp feature increases and/or the broad feature decreases in intensity with O_2 dosing. For paramagnetic systems, however, observed NMR spectral intensities are generally not quantitative due to rapid spin-lattice (T_1) and spin-spin (T_2) relaxation. For purposes of quantitation, we therefore measured both the ^{23}Na T_1 and T_2 relaxation times, as shown in Figures S10 and S11. The VOCS spectra are quantitative with respect to T_1 relaxation but not T_2 relaxation. In particular, across all samples, the broad feature has a very short T_2 time (on the order of 500 μs), such that between 35% and 55% of its intensity (depending on the specific sample) is lost prior to acquisition. Correcting the intensity of both deconvoluted signals using the measured T_2 times gives quantitative relative intensities (Figure 5b). The broad feature contributes to 75% of the total spectral intensity for the undosed sample, and the relative intensity of the peak decreases to 61% and 45% in the samples dosed with O_2 at 298 and 473 K, respectively. Conversely, the relative intensity of the sharp component increases from 25% in the activated framework to 39% and 55% in the samples dosed with O_2 at 298 and 473 K, respectively.

These spectral trends imply that the broad feature corresponds to ^{23}Na sites in the reduced structure that are not interacting with oxygen. The sharp component therefore appears to correspond to a chemically distinct environment associated with incorporated oxygen. Though the chemical shift of the sharp component at −12 ppm is in the vicinity of the known room-temperature ^{23}Na shift of NaO_2 (−30 ppm),[48] this feature is clearly observed even for the undosed sample and therefore cannot be assigned *exclusively* to superoxo-associated Na^+. We hypothesize that this feature in the undosed spectrum corresponds to Na^+ near oxygen-containing ligand-vacancy defects that are clearly observed in the XPS data (for reference, the ^{23}Na shift of sodium formate is ~0 ppm).[50] We also expect a smaller degree of spin density transfer from Fe to ligand vacancy sites, leading to a sharper ^{23}Na signal for associated Na^+ relative to the signal arising from sodium ions in the rest of the framework.

In the O_2-dosed samples, then, the sharp feature likely comprises multiple sites, a conclusion supported by analysis of the spinning sideband intensities. In particular, were this feature due only to a single type of Na^+ site in the activated framework that becomes more predominant with O_2 dosing, the intensity of its spinning sideband manifold should remain proportional to that of the centerband. Instead, the spinning sidebands comprise 65% of the total intensity of this feature in the undosed spectrum but only 48% and 45% of the feature in the dosed spectra at 298 and 473 K, respectively. Additional support comes from the T_1 measurements (Figure S10): the sharp component exhibits monoexponential relaxation for the undosed sample, suggesting a single site, whereas after O_2 dosing the relaxation behavior is bi- or multiexponential, indicating multiple distinct environments with differing T_1 times. We conclude that, with O_2 dosing, a second type of Na^+ site that we assign to Na^+ positioned near superoxo species begins to dominate the observed intensity of the sharp component centered at −12 ppm. However, paramagnetic broadening leading to a fwhm of ~50 ppm of the sharp component as well as the differing chemical nature of the sodium environment(s) in this system relative to either sodium formate or sodium superoxide mean that deconvolution or distinction by chemical shift alone are not possible, due to likely overlap between the signal observed from Na^+ near defects and Na^+ near superoxo species.

To corroborate the sign and magnitude of the assigned ^{23}Na NMR shifts, we performed DFT calculations on a small cluster model (Figure S12) generated from the refined single-crystal structure of the O_2-dosed sodiated framework (Figure 1). Many of the linkers were further converted to non-bridging phenyl pyrazolate units to minimize the system size, while still capturing the local sodium ion environments. The calculated isotropic hyperfine coupling constants for the ^{23}Na sites were found to be small and negative, and by using the experimental magnetic susceptibility data (see below), they could be further scaled[51,52] to obtain room-temperature Fermi contact shifts between −9 and −20 ppm. This shift range is in good agreement with the experimental ^{23}Na shift of the sharp component at −12 ppm, ascribed to Na^+ sites near reduced O_2 species (and/or defects). These calculations suggest that, despite the highly paramagnetic

nature of the framework, the ^{23}Na nuclei do not experience a significant Fermi contact shift, due to the relatively weak Na^+···framework interactions. Moreover, the calculations confirm that the nearby O_2 species does not induce large ^{23}Na Fermi contact shifts. We note that experimental ^{23}Na NMR characterization of sodium superoxide similarly found the absence of a significant ^{23}Na Fermi contact shift.[48]

Finally, we performed static and MAS solid-state ^{17}O NMR spectroscopy after dosing an activated sample of $Na_{1.04}Fe_2(bdp)_3$ with ^{17}O-enriched O_2 (see Supporting Information). We did not observe signal in these experiments even after long signal averaging times of ~12 h, suggesting the speciation of O_2 as paramagnetic superoxide rather than diamagnetic peroxide. We note that while ^{17}O NMR spectra of alkali metal peroxides have been reported, this is not the case for the corresponding superoxides,[48] as the unpaired spin localized on the NMR-active nucleus renders spectral acquisition extremely challenging. Taken together, the ^{23}Na and ^{17}O solid-state NMR data support the hypothesis that, upon O_2 dosing, the Na^+ ions move slightly further from the linkers to accommodate and associate with O_2, which is incorporated as a superoxide guest species.

O_2 Adsorption in More-Reduced $Fe_2(bdp)_3$ and in an Expanded-Pore Analogue.

Measurable porosity is still observed for O_2-dosed $K_{1.02}Fe_2(bdp)_3$ (Figure S13), suggesting that restricted O_2 diffusion—potentially due to pore occlusion by reduced O_2 species—does not completely explain the apparent kinetically limited O_2 adsorption at ambient temperature. To further investigate the possible restriction of O_2 diffusion, we prepared a more reduced form of the framework material, $K_{1.88}Fe_2(bdp)_3$, as well as an expanded-pore analogue $Fe_2(bpeb)_3$ ($bpeb^{2-}$ = 1,4-bis(pyrazolide-4-ylethynyl)benzene)[53] (see below). In the more reduced material, the pores should be even more occluded and O_2 diffusion more restricted. Indeed, as noted above, this material is essentially nonporous to N_2 at 77 K, with a Langmuir surface area of only ~70 m^2/g (Figure S14). As such, if O_2 diffusion represents the primary kinetic barrier to O_2 adsorption, it would be expected that the fully reduced material should show far lower O_2 uptake.

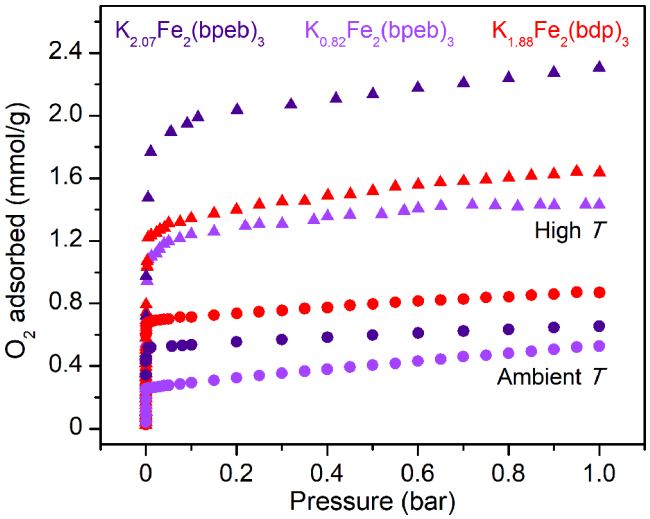

Figure 6. Adsorption isotherms for the uptake of O_2 at 298 K for $K_{1.88}Fe_2(bdp)_3$, $K_{0.82}Fe_2(bpeb)_3$, and $K_{2.07}Fe_2(bpeb)_3$ (red, light purple, and dark purple filled circles, respectively). Adsorption of O_2 at elevated temperature is shown with triangles. $K_{1.88}Fe_2(bdp)_3$ was measured at 473 K whereas the expanded pore analogues were measured at 453 K.

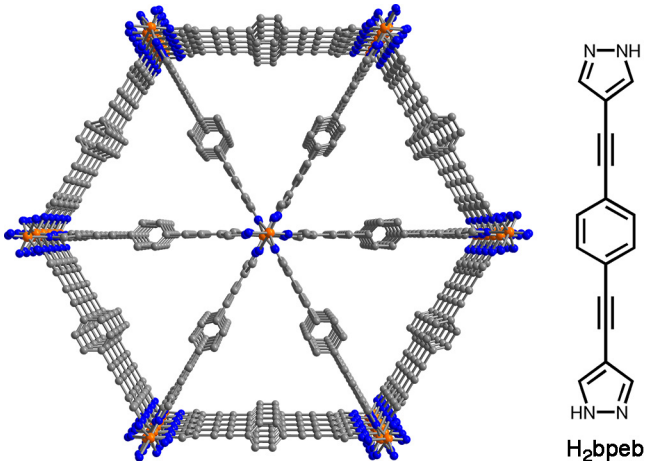

Figure 7. (Left) Solid-state structure of $Fe_2(bpeb)_3$.[53] Orange, blue, and gray spheres represent Fe, N, and C atoms, respectively. H atoms are omitted for clarity. (Right) The organic linker H_2bpeb.

At 298 K, $K_{1.88}Fe_2(bdp)_3$ exhibits steep initial O_2 uptake to a loading of 0.68 mmol/g at ~6 mbar that then tapers off to yield a loading of 0.87 mmol/g at 1 bar (Figure 6). Significantly, for all pressures measured, the O_2 capacities are higher than those in the half-reduced material. As observed for $K_{1.09}Fe_2(bdp)_3$, the O_2 loading at 0.21 bar is far lower than the theoretical capacity of 2.46 mmol/g. However, since this material adsorbs an appreciable quantity of O_2, it is unlikely that restricted diffusion is the primary reason for the apparent kinetic control of O_2 adsorption. When dosed with O_2 at 473 K, $K_{1.88}Fe_2(bdp)_3$ again exhibits steep uptake with even greater capacities of 1.23, 1.40, and 1.64 mmol/g at 10 mbar, 0.21 bar, and 1 bar, respectively, suggesting the fully reduced framework operates under similar kinetic limitations as the half-reduced form. Despite the overall improvement in capacity at elevated temperature, the uptake in $K_{1.88}Fe_2(bdp)_3$ near atmospheric oxygen partial pressure is only ~60% of its theoretical capacity, whereas $K_{1.09}Fe_2(bdp)_3$ achieves approximately 80% under similar conditions. This result indicates that increased kinetic limitations may occur with increasing reduction above $K_{1.09}Fe_2(bdp)_3$—such as more restricted movement of cations or sluggish rearrangement of reduced O_2 species. Additionally, it is possible that different redox behavior for the fully reduced material[29] could lead to partial formation of more reduced O_2^{n-} products.

The framework $Fe_2(bpeb)_3$[53] features larger interchain separations relative to $Fe_2(bdp)_3$, (18.2 versus 13.2 Å, respectively; Figure 7), which give rise to larger pores that should reduce or preclude restricted O_2 diffusion. Additionally, this framework displays thermal stability above 350 °C in air, although it is less stable in the presence of water relative to $Fe_2(bdp)_3$.[53] We prepared H_2bpeb according to reported procedures[53,54] and synthesized $Fe_2(bpeb)_3$ in an analogous manner to $Fe_2(bdp)_3$. Notably, we determined a Langmuir surface area of 2270 m^2/g for this expanded material (Figure S15), far higher than the previously reported value of 1600 m^2/g.[53] Treatment of $Fe_2(bpeb)_3$ with potassium naphthalenide aimed at half and full reduction yielded $K_{0.82}Fe_2(bpeb)_3$ and $K_{2.07}Fe_2(bpeb)_3$, respectively. Powder X-ray diffraction data confirmed topotactic reduction of $Fe_2(bpeb)_3$ (Figure S16) as well as adsorption of O_2 without significant loss in crystallinity or changes in symmetry (Figure S17).

Interestingly, the 298-K O_2 adsorption behavior of $K_{0.82}Fe_2(bpeb)_3$ is very similar to that of $K_{1.09}Fe_2(bdp)_3$, despite its substantially higher Langmuir surface area (1700 m^2/g

compared to ~750 m^2/g, respectively; Figure S18) and much larger pore diameter. After an initial steep uptake until ~1 mbar (reaching a loading of 0.26 mmol/g; Figure 6), the capacity increases gradually with loading to 0.33 mmol/g close to 0.21 bar of O_2 and 0.53 mmol/g at 1 bar. These loadings correspond to 37% and 59% of the theoretical capacity, respectively. The similarities in O_2 adsorption behavior between $K_{0.82}Fe_2(bpeb)_3$ and $K_{1.09}Fe_2(bdp)_3$ continue at higher temperature, where at 453 K, the expanded-pore material exhibits steep uptake and greater capacities of 1.10, 1.29, and 1.43 mmol/g at 12 mbar, 0.21 bar, and 1 bar, respectively. Note that 453 K represents the activation temperature of the reduced framework and was chosen for this measurement as it should produce very similar behavior to data obtained at 473 K for $A_xFe_2(bdp)_3$ without increasing the risk of framework degradation for the expanded-pore analogue.

Similar behavior is also observed for the fully reduced compound $K_{2.07}Fe_2(bpeb)_3$, which exhibits a Langmuir surface area of 600 m^2/g (Figure S19). For this material, the K:Fe ratio is slightly greater than 1, which can likely be ascribed to a combination of metals analysis measurement error and defect site reduction. Sharp O_2 adsorption occurs in this framework at 298 K until ~5 mbar, corresponding to a loading of 0.52 mmol/g, and loadings of 0.55 and 0.65 mmol/g are achieved close to 0.21 bar and at 1 bar, respectively (Figure 6). At 453 K, 1.9 mmol/g O_2 is adsorbed at 50 mbar and 2.3 mmol/g at 1 bar. Notably, though the O_2 uptake of $K_{2.07}Fe_2(bpeb)_3$ at 298 K and ~0.21 bar corresponds to only 26% of its theoretical capacity, at 453 K and ~0.21 bar, the material is capable of adsorbing 93% of its theoretical capacity. These results for the expanded-pore system indicate that there still appears to be some form of kinetic control over the adsorption of O_2 that is almost certainly not associated with restriction of O_2 diffusion. Indeed, if diffusion was the solely limiting factor for O_2 uptake, we would expect the quantity of adsorbed gas to be independent of temperature for $Fe_2(bpeb)_3$, wherein the large pores should dramatically reduce or eliminate any restriction of diffusion.

Electronic and Magnetic Properties of $KFe_2(bdp)_3$ and O_2-dosed $KFe_2(bdp)_3$.

To further examine O_2 adsorption behavior in chemically reduced $Fe_2(bdp)_3$, we turned to a combination of ^{57}Fe Mössbauer spectroscopy and magnetic susceptibility measurements.

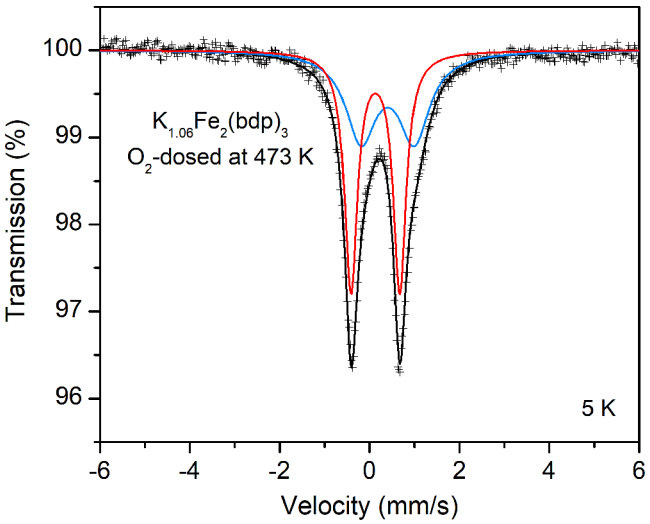

Figure 8. The 5-K Mössbauer spectrum for a sample of $K_{1.06}Fe_2(bdp)_3$ dosed with 1 bar O_2 at 473 K. The red and blue doublet fits correspond to low-spin Fe^{III} and a previously unobserved Fe species, respectively.

Mössbauer analysis has been used previously to confirm the increasing presence of high-spin Fe^{II} centers as well as a high degree of electron delocalization with increased chemical reduction of $Fe_2(bdp)_3$.[29] The 5-K Mössbauer spectrum for a sample of $K_{1.06}Fe_2(bdp)_3$ dosed with O_2 at 473 K (i.e., the most oxidized, O_2-rich sample) reveals two distinct Fe environments (Figure 8). The primary spectral feature has an isomer shift of 0.129(2) mm/s that matches the shift for $Fe_2(bdp)_3$ (Fe^{III}, $\langle\delta\rangle$ = 0.129(1) mm/s) and is distinct from the shift for $K_{1.1}Fe_2(bdp)_3$ (Fe^{III}, $\langle\delta\rangle$ = 0.214(5) mm/s).[29] This result indicates that the introduction of O_2 causes electron transfer from the reduced framework, resulting in re-oxidation of the iron centers back to low-spin Fe^{III}. The isomer shift of the second feature is 0.42(2) mm/s, which is considerably lower than the value reported for Fe^{II} in $K_{1.1}Fe_2(bdp)_3$, and is indicative of a new electronic environment. The exact nature of this species remains unclear, but the signal could correspond to remnant low-spin Fe^{II}. Another assignment consistent with this second feature is high-spin Fe^{III}.[55] In either case, interactions between pore-dwelling superoxo species and the framework may also contribute to the observed signal parameters. The full assignment of this signal and complete understanding of the complex electronic and magnetic structure in either reduced $Fe_2(bdp)_3$ or its O_2-dosed congeners is beyond the scope of this work, but a more detailed discussion of the Mössbauer measurements can be found in the Supporting Information. The Mössbauer spectrum for $K_{1.06}Fe_2(bdp)_3$ dosed with O_2 at ambient temperature is very similar (Figure S22), displaying two distinct features with similar isomer shifts and quadrupole splittings as those for the sample dosed at 473 K. Both datasets indicate that $K_{1.06}Fe_2(bdp)_3$ is substantially re-oxidized in the presence of O_2 and features a new iron electronic environment.

Given the paramagnetic nature of both the framework and the observed superoxo species, we further investigated the electronic structure of activated and O_2-dosed samples of $K_{1.06}Fe_2(bdp)_3$ using magnetic susceptibility measurements (Figure 9). At 300 K, the value of the molar magnetic susceptibility times temperature ($\chi_M T$) for the activated sample is 3.19 emu·K/mol, while a Curie-Weiss fit of the inverse susceptibility versus temperature (Figure S25) over the range 85 to 300 K yielded values of C = 3.51 emu·K/mol and θ_{CW} = −33 K. Notably, this value of C is close to the value of 3.53 emu·K/mol

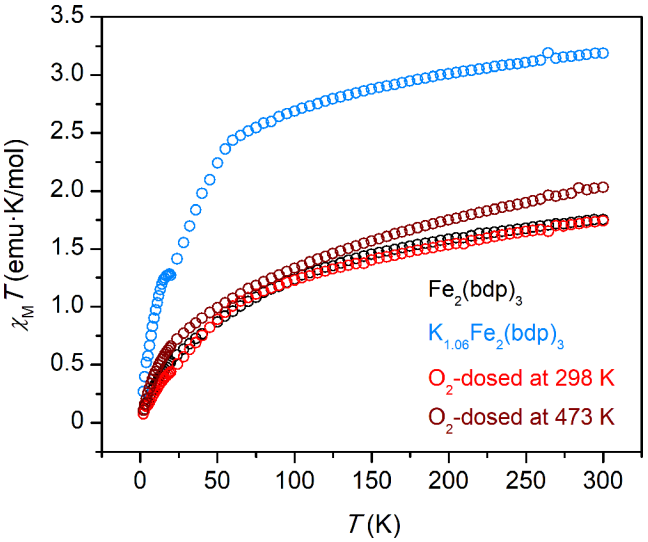

Figure 9. Variable-temperature molar magnetic susceptibility times temperature ($\chi_M T$) versus T obtained at 7 T for $Fe_2(bdp)_3$ (black), $K_{1.06}Fe_2(bdp)_3$ (blue), and $K_{1.06}Fe_2(bdp)_3$ dosed with 1 bar of O_2 at 298 K (red), and 473 K (dark red).

expected if the added electrons result in the conversion of low-spin Fe^{III} sites to high-spin Fe^{II} sites. However, this result differs from our previously reported Mössbauer spectroscopy results, which show a small fraction of high-spin Fe^{II} in the half-reduced framework.[29] As such, the large $\chi_M T$ value of the sample may indicate the presence of clusters of low-spin Fe^{III} centers strongly coupled by conduction electrons, although further measurements are needed to understand fully the magnetic structure of this material.

Both the ambient-temperature and high-temperature O_2-dosed samples exhibit lower $\chi_M T$ values of 1.74 and 2.03 emu·K/mol, respectively, compared to the activated sample (Figure 9), consistent with the removal of conduction electrons upon electron transfer to adsorbed O_2. Importantly, the larger $\chi_M T$ value of the high-temperature dosed sample is consistent with an increased concentration of S = 1/2 superoxo species within the pores of the framework. Indeed, the room-temperature $\chi_M T$ value of this sample is 0.29 emu·K/mol larger than the room temperature moment of $Fe_2(bdp)_3$, reasonably close to the expected increase of 0.32 emu·K/mol, assuming one S = 1/2 spin per adsorbed O_2 and no change in the moment of the host framework. Unfortunately, quantitative analysis of the magnetic susceptibility of these samples is complicated by contributions from temperature-independent paramagnetism (Figure S26), even under an applied field of 7 T, as was previously observed for $Fe_2(bdp)_3$. However, the data qualitatively agree with the formation of an S = 1/2 superoxo species upon adsorption of O_2.

O_2 Adsorption Mechanism.

The foregoing results from gas adsorption, X-ray diffraction, spectroscopic, and magnetic susceptibility experiments provide a consistent picture for the mechanism of O_2 adsorption in these chemically reduced Fe^{III}-pyrazolate frameworks. Upon introduction of O_2 even at very low pressures, the strongly reducing framework drives what is ostensibly outer-sphere electron transfer, thereby reducing O_2 to a superoxide (O_2^-) guest species, followed by movement of this reduced species to a more favorable binding position stabilized by the alkali metal cations residing within the pores. The theoretical O_2 uptake expected for this mechanism is not realized at 298 K due to a kinetic limitation. This kinetic limitation is almost certainly not due to the restriction of O_2 diffusion resulting from pore occlusion by reduced O_2 species. Instead, it is likely a result of a large reorganization energy associated with rearrangement of the alkali cations from their preferred positions prior to O_2 dosing and/or the movement and ordering of superoxo species after O_2 reduction. This explanation seems especially plausible when considering the crystal structures of the O_2-loaded frameworks. The alkali metal cation sites that stabilize the O_2 species are over 1.2 Å away from the other alkali metal sites that interact with the ligand phenyl rings and the reduced O_2 species are positioned relatively far away from the iron centers. These distances imply large degrees of rearrangement after reduction of O_2 and suggest that back-transfer of electrons from the reduced O_2 species to the framework may also be subject to such a barrier, requiring significant thermal energy for framework regeneration. One possible approach to enhance the cycling ability of the material would thus be to employ cations that could enhance O_2 reduction by positioning reduced O_2 species much closer to the framework. These templating cations might also facilitate the reversal of this reduction.

Conclusion

Molecular complexes and materials such as metal–organic frameworks that reversibly bind dioxygen traditionally do so at coordinatively unsaturated, redox-active metal sites, which transfer an electron to O_2 by an inner-sphere mechanism.[9-12,23-27] Here, we have presented an alternative strategy for the selective capture of O_2, via outer-sphere electron transfer to O_2 from a robust, chemically reduced framework with coordinatively saturated, redox-active metal sites. Through a suite of characterization techniques, we have shown that the O_2 species adsorbed in $A_xFe_2(bdp)_3$ (A = Na^+, K^+) are superoxide moieties stabilized by sodium or potassium cations. The deeper understanding gained here of a relatively unexplored mechanism of O_2 reduction and binding is of fundamental interest, yet these results can also inform the design of new O_2 selective adsorbents for numerous industries and important pre- and post-combustion carbon capture technologies that require high-purity oxygen.

ASSOCIATED CONTENT

The Supporting Information is available free of charge.

Synthesis and characterization details, and details of gas adsorption, spectroscopic, and diffraction measurements and analysis.

Crystallographic information files (CIFs) for $Na_{1.2}Fe_2(bdp)_3$ and $K_{0.74}Fe_2(bdp)_3$ have been deposited in the Cambridge Crystallographic Data Centre under deposition numbers 2007874 and 2007875, respectively.

AUTHOR INFORMATION

Corresponding Author

*jrlong@berkeley.edu

ORCID

Adam Jaffe: 0000-0002-9886-0249
Michael E. Ziebel: 0000-0003-1857-8292
David M. Halat: 0000-0002-0919-1689
Naomi Biggins: 0000-0002-4132-6395
Ryan A. Murphy: 0000-0002-3695-2295
Khetpakorn Chakarawet: 0000-0001-5905-3578
Jeffrey A. Reimer: 0000-0002-4191-3725
Jeffrey R. Long: 0000-0002-5324-1321

Notes

These authors declare no competing financial interest

ACKNOWLEDGMENT

This work was supported by the U.S. Department of Energy (DOE), Office of Science, Office of Basic Energy Sciences, under Award DE-SC0019992. Single-crystal X-ray diffraction data were collected at Beamline 12.2.1 at the Advanced Light Source at Lawrence Berkeley National Laboratory. This research used resources of the Advanced Light Source, which is a DOE Office of Science User Facility under contract no. DE-AC02-05CH11231. XPS spectra were acquired at the Biomolecular Nanotechnology Center/QB3 at UC Berkeley. Powder X-ray diffraction data were collected on the 17-BM-B Beamline at the Advanced Photon Source (APS), a U.S. Department of Energy Office of Science User Facility operated by Argonne National Laboratory. Use of the Advanced Photon Source at Argonne National Laboratory was supported by the U.S. Department of Energy, Office of Science, Office of Basic Energy Sciences, under Contract No. DE-AC02-06CH11357. Density functional theory calculations implemented through Gaussian 16 code were supported by the Molecular Graphics and Computation Facility of the UC Berkeley College of Chemistry that is

supported by NIH S10OD023532. We thank Prof. Christopher J. Chang at UC Berkeley for the use of the Mössbauer spectrometer and the UC Berkeley College of Chemistry NMR Facility (supported in part by NIH S10OD024998) and Dr. Hasan Celik for assistance with NMR instrumentation. We also thank Julia Oktawiec and Maria Paley for assistance with powder X-ray diffraction collection at the APS. We thank the National Institute of General Medical Sciences of the National Institutes of Health for support of A.J. through a postdoctoral fellowship under Award Number F32GM131587. The content is solely the responsibility of the authors and does not necessarily represent the official views of the National Institutes of Health. D.M.H. acknowledges support from the Joint Center for Energy Storage Research, an Energy Innovation Hub funded by the U.S. Department of Energy, Office of Science, Basic Energy Sciences. We are grateful to Dr. Benjamin Snyder for helpful discussion of the Mössbauer results, Dr. Alexander Forse for helpful discussion of the NMR experiments, and Dr. Katie Meihaus and Dr. T. David Harris for editorial assistance.

REFERENCES

(1) Olajire, A. A. CO_2 capture and separation technologies for end-of-pipe applications – A review. *Energy* **2010**, *35*, 2610-2628.
(2) Kirschner, M. J.; Alekseev, A.; Dowy, S.; Grahl, M.; Jansson, L.; Keil, P.; Lauermann, G.; Meilinger, M.; Schmehl, W.; Weckler, H.; Windmeier, C. In *Ullmann's Encyclopedia of Industrial Chemistry*; Wiley–VCH Verlag GmbH & Co. KGaA: Weinheim, 2017.
(3) Smith, A. R.; Klosek, J. A review of air separation technologies and their integration with energy conversion processes. *Fuel Process. Technol.* **2001**, *70*, 115-134.
(4) Gaffney, T. R. Porous solids for air separation. *Curr. Opin. Solid State Mater. Sci.* **1996**, *1*, 69-75.
(5) Wu, C.-W.; Kothare, M. V.; Sircar, S. Equilibrium Adsorption Isotherms of Pure N_2 and O_2 and Their Binary Mixtures on LiLSX Zeolite: Experimental Data and Thermodynamic Analysis. *Ind. Eng. Chem. Res.* **2014**, *53*, 7195-7201.
(6) Jansen, D.; Gazzani, M.; Manzolini, G.; Dijk, E. v.; Carbo, M. Precombustion CO_2 capture. *Int. J. Greenhouse Gas Control* **2015**, *40*, 167-187.
(7) Pardemann, R.; Meyer, B. In *Handbook of Clean Energy Systems*; Yan, J., Ed.; John Wiley & Sons, Ltd.: 2015.
(8) Li, J.-R.; Kuppler, R. J.; Zhou, H.-C. Selective gas adsorption and separation in metal-organic frameworks. *Chem. Soc. Rev.* **2009**, *38*, 1477-1504.
(9) Niederhoffer, E. C.; Timmons, J. H.; Martell, A. E. Thermodynamics of oxygen binding in natural and synthetic dioxygen complexes. *Chem. Rev.* **1984**, *84*, 137-203.
(10) Jones, R. D.; Summerville, D. A.; Basolo, F. Synthetic oxygen carriers related to biological systems. *Chem. Rev.* **1979**, *79*, 139-179.
(11) Li, G. Q.; Govind, R. Separation of Oxygen from Air Using Coordination Complexes: A Review. *Ind. Eng. Chem. Res.* **1994**, *33*, 755-783.
(12) Southon, P. D.; Price, D. J.; Nielsen, P. K.; McKenzie, C. J.; Kepert, C. J. Reversible and Selective O_2 Chemisorption in a Porous Metal–Organic Host Material. *J. Am. Chem. Soc.* **2011**, *133*, 10885-10891.
(13) Li, J.-R.; Sculley, J.; Zhou, H.-C. Metal–Organic Frameworks for Separations. *Chem. Rev.* **2012**, *112*, 869-932.
(14) Sumida, K.; Rogow, D. L.; Mason, J. A.; McDonald, T. M.; Bloch, E. D.; Herm, Z. R.; Bae, T.-H.; Long, J. R. Carbon Dioxide Capture in Metal–Organic Frameworks. *Chem. Rev.* **2012**, *112*, 724-781.
(15) Herm, Z. R.; Bloch, E. D.; Long, J. R. Hydrocarbon Separations in Metal–Organic Frameworks. *Chem. Mater.* **2014**, *26*, 323-338.
(16) Schneemann, A.; Bon, V.; Schwedler, I.; Senkovska, I.; Kaskel, S.; Fischer, R. A. Flexible metal–organic frameworks. *Chem. Soc. Rev.* **2014**, *43*, 6062-6096.
(17) Furukawa, H.; Cordova, K. E.; O′Keeffe, M.; Yaghi, O. M. The Chemistry and Applications of Metal-Organic Frameworks. *Science* **2013**, *341*.
(18) Guillerm, V.; Kim, D.; Eubank, J. F.; Luebke, R.; Liu, X.; Adil, K.; Lah, M. S.; Eddaoudi, M. A supermolecular building approach for the design and construction of metal–organic frameworks. *Chem. Soc. Rev.* **2014**, *43*, 6141-6172.
(19) Howarth, A. J.; Liu, Y.; Li, P.; Li, Z.; Wang, T. C.; Hupp, J. T.; Farha, O. K. Chemical, thermal and mechanical stabilities of metal–organic frameworks. *Nat. Rev. Mater.* **2016**, *1*, 15018.
(20) Férey, G. Some suggested perspectives for multifunctional hybrid porous solids. *Dalton Trans.* **2009**, 4400-4415.
(21) Horike, S.; Umeyama, D.; Kitagawa, S. Ion Conductivity and Transport by Porous Coordination Polymers and Metal – Organic Frameworks. *Acc. Chem. Res.* **2013**, *46*, 2376-2384.
(22) Bon, V.; Brunner, E.; Pöppl, A.; Kaskel, S. Unraveling Structure and Dynamics in Porous Frameworks via Advanced In Situ Characterization Techniques. *Adv. Funct. Mater.* **2020**, 1907847.
(23) Murray, L. J.; Dinca, M.; Yano, J.; Chavan, S.; Bordiga, S.; Brown, C. M.; Long, J. R. Highly-Selective and Reversible O_2 Binding in Cr_3(1,3,5-benzenetricarboxylate)$_2$. *J. Am. Chem. Soc.* **2010**, *132*, 7856-7857.
(24) Bloch, E. D.; Queen, W. L.; Hudson, M. R.; Mason, J. A.; Xiao, D. J.; Murray, L. J.; Flacau, R.; Brown, C. M.; Long, J. R. Hydrogen Storage and Selective, Reversible O_2 Adsorption in a Metal–Organic Framework with Open Chromium(II) Sites. *Angew. Chem., Int. Ed.* **2016**, *55*, 8605-8609.
(25) Bloch, E. D.; Murray, L. J.; Queen, W. L.; Chavan, S.; Maximoff, S. N.; Bigi, J. P.; Krishna, R.; Peterson, V. K.; Grandjean, F.; Long, G. J.; Smit, B.; Bordiga, S.; Brown, C. M.; Long, J. R. Selective Binding of O_2 over N_2 in a Redox–Active Metal–Organic Framework with Open Iron(II) Coordination Sites. *J. Am. Chem. Soc.* **2011**, *133*, 14814-14822.
(26) Xiao, D. J.; Gonzalez, M. I.; Darago, L. E.; Vogiatzis, K. D.; Haldoupis, E.; Gagliardi, L.; Long, J. R. Selective, Tunable O_2 Binding in Cobalt(II) – Triazolate/Pyrazolate Metal – Organic Frameworks. *J. Am. Chem. Soc.* **2016**, *138*, 7161-7170.
(27) Gallagher, A. T.; Lee, J. Y.; Kathiresan, V.; Anderson, J. S.; Hoffman, B. M.; Harris, T. D. A structurally-characterized peroxomanganese(IV) porphyrin from reversible O_2 binding within a metal-organic framework. *Chem. Sci.* **2018**, *9*, 1596-1603.
(28) Herm, Z. R.; Wiers, B. M.; Mason, J. A.; van Baten, J. M.; Hudson, M. R.; Zajdel, P.; Brown, C. M.; Masciocchi, N.; Krishna, R.; Long, J. R. Separation of Hexane Isomers in a Metal-Organic Framework with Triangular Channels. *Science* **2013**, *340*, 960-964.
(29) Aubrey, M. L.; Wiers, B. M.; Andrews, S. C.; Sakurai, T.; Reyes-Lillo, S. E.; Hamed, S. M.; Yu, C.-J.; Darago, L. E.; Mason, J. A.; Baeg, J.-O.; Grandjean, F.; Long, G. J.; Seki, S.; Neaton, J. B.; Yang, P.; Long, J. R. Electron delocalization and charge mobility as a function of reduction in a metal–organic framework. *Nat. Mater.* **2018**, *17*, 625-632.
(30) Xie, L. S.; Sun, L.; Wan, R.; Park, S. S.; DeGayner, J. A.; Hendon, C. H.; Dincă, M. Tunable Mixed-Valence Doping toward Record Electrical Conductivity in a Three-Dimensional Metal–Organic Framework. *J. Am. Chem. Soc.* **2018**, *140*, 7411-7414.
(31) Jackson, C. B.; Werner, R. C. In *Handling and Uses of the Alkali Metals*; American Chemical Society: 1957; Vol. 19, p. 174-177.
(32) Sawyer, D. T.; Valentine, J. S. How super is superoxide? *Acc. Chem. Res.* **1981**, *14*, 393-400.
(33) Hayyan, M.; Hashim, M. A.; AlNashef, I. M. Superoxide Ion: Generation and Chemical Implications. *Chem. Rev.* **2016**, *116*, 3029-3085.
(34) Myers, A. L.; Prausnitz, J. M. Thermodynamics of mixed-gas adsorption. *AlChE J.* **1965**, *11*, 121-127.
(35) Walton, K. S.; Sholl, D. S. Predicting multicomponent adsorption: 50 years of the ideal adsorbed solution theory. *AlChE J.* **2015**, *61*, 2757-2762.
(36) Biggins, N.; Ziebel, M. E.; Gonzalez, M. I.; Long, J. R. Crystallographic Characterization of the Metal – Organic Framework Fe_2(bdp)$_3$ upon Reductive Cation Insertion. *ChemRxiv* **2020**, DOI: 10.26434/chemrxiv.12501842.v1
(37) Dupin, J.-C.; Gonbeau, D.; Vinatier, P.; Levasseur, A. Systematic XPS studies of metal oxides, hydroxides and peroxides. *Phys. Chem. Chem. Phys.* **2000**, *2*, 1319-1324.
(38) Sherwood, P. M. A. The use and misuse of curve fitting in the analysis of core X-ray photoelectron spectroscopic data. *Surf. Interface Anal.* **2019**, *51*, 589-610.
(39) Sexton, B. A.; Hughes, A. E. A comparison of weak molecular adsorption of organic molecules on clean copper and platinum surfaces. *Surf. Sci.* **1984**, *140*, 227-248.
(40) Younesi, R.; Hahlin, M.; Björefors, F.; Johansson, P.; Edström, K. Li–O_2 Battery Degradation by Lithium Peroxide (Li_2O_2): A Model Study. *Chem. Mater.* **2013**, *25*, 77-84.
(41) Bournel, F.; Laffon, C.; Parent, P.; Tourillon, G. Adsorption of some substituted ethylene molecules on Pt(111) at 95 K Part 1: NEXAFS, XPS and UPS studies. *Surf. Sci.* **1996**, *350*, 60-78.
(42) Moulder, J. F.; Stickle, W. F.; Sobol, P. E.; Bomben, K. D. *Handbook of X-ray Photoelectron Spectroscopy*; Chastain, J., Ed.; Physical

Electronics Division, Perkin-Elmer Corporation: Eden Prairie, Minnesota, 1992.
(43) Puglia, C.; Bennich, P.; Hasselström, J.; Brühwiler, P. A.; Nilsson, A.; Li, Z. Y.; Rudolf, P.; Mårtensson, N. XPS and XAS study of oxygen coadsorbed with a dispersed phase of K on graphite. *Surf. Sci.* **2001**, *488*, 1-6.
(44) Wood, K. N.; Teeter, G. XPS on Li-Battery-Related Compounds: Analysis of Inorganic SEI Phases and a Methodology for Charge Correction. *ACS Appl. Energy Mater.* **2018**, *1*, 4493-4504.
(45) Lamontagne, B.; Semond, F.; Roy, D. X-ray photoelectron spectroscopic study of Si(111) oxidation promoted by potassium multilayers under low O_2 pressures. *J. Electron. Spectrosc. Relat. Phenom.* **1995**, *73*, 81-88.
(46) Pell, A. J.; Pintacuda, G.; Grey, C. P. Paramagnetic NMR in solution and the solid state. *Prog. Nucl. Magn. Reson. Spectrosc.* **2019**, *111*, 1-271.
(47) Smiley, D. L.; Carlier, D.; Goward, G. R. Combining density functional theory and ^{23}Na NMR to characterize Na_2FePO_4F as a potential sodium ion battery cathode. *Solid State Nucl. Magn. Reson.* **2019**, *103*, 1-8.
(48) Krawietz, T. R.; Murray, D. K.; Haw, J. F. Alkali Metal Oxides, Peroxides, and Superoxides: A Multinuclear MAS NMR Study. *J. Phys. Chem. A* **1998**, *102*, 8779-8785.
(49) Tong, Y. Y. Nuclear Spin-Echo Fourier-Transform Mapping Spectroscopy for Broad NMR Lines in Solids. *J. Magn. Reson., Ser A* **1996**, *119*, 22-28.
(50) Ryoko, T.; Hazime, S. ^{23}Na Chemical Shifts of Some Inorganic and Organic Compounds in the Solid State as Determined by the Magic Angle Spinning and High Power NMR Methods. *Chem. Lett.* **1984**, *13*, 293-296.
(51) Middlemiss, D. S.; Ilott, A. J.; Clément, R. J.; Strobridge, F. C.; Grey, C. P. Density Functional Theory-Based Bond Pathway Decompositions of Hyperfine Shifts: Equipping Solid-State NMR to Characterize Atomic Environments in Paramagnetic Materials. *Chem. Mater.* **2013**, *25*, 1723-1734.
(52) Wu, Y.; Halat, D. M.; Wei, F.; Binford, T.; Seymour, I. D.; Gaultois, M. W.; Shaker, S.; Wang, J.; Grey, C. P.; Cheetham, A. K. Mixed X-Site Formate−Hypophosphite Hybrid Perovskites. *Chem. Eur. J.* **2018**, *24*, 11309-11313.
(53) Galli, S.; Maspero, A.; Giacobbe, C.; Palmisano, G.; Nardo, L.; Comotti, A.; Bassanetti, I.; Sozzani, P.; Masciocchi, N. When long bis(pyrazolates) meet late transition metals: structure, stability and adsorption of metal-organic frameworks featuring large parallel channels. *J. Mater. Chem. A* **2014**, *2*, 12208-12221.
(54) Padial, N. M.; Quartapelle Procopio, E.; Montoro, C.; López, E.; Oltra, J. E.; Colombo, V.; Maspero, A.; Masciocchi, N.; Galli, S.; Senkovska, I.; Kaskel, S.; Barea, E.; Navarro, J. A. R. Highly Hydrophobic Isoreticular Porous Metal–Organic Frameworks for the Capture of Harmful Volatile Organic Compounds. *Angew. Chem., Int. Ed.* **2013**, *52*, 8290-8294.
(55) Mbughuni, M. M.; Chakrabarti, M.; Hayden, J. A.; Bominaar, E. L.; Hendrich, M. P.; Münck, E.; Lipscomb, J. D. Trapping and spectroscopic characterization of an Fe^{III}-superoxo intermediate from a nonheme mononuclear iron-containing enzyme. *Proc. Natl. Acad. Sci. U.S.A.* **2010**, *107*, 16788-16793.

For Table of Contents Only